SAND99-2735J

Extending molecular theory to steady-state diffusing systems

Laura J. Douglas Frink* and Aidan Thompson
Computational Biology and Materials Technology Department
Sandia National Laboratories
Albuquerque, New Mexico 87185-1111

Andrew G. Salinger
Parallel Computational Sciences Department
Sandia National Laboratories
Albuquerque, New Mexico 87185-1111

(October 8, 1999)

Predicting the properties of nonequilibrium systems from molecular simulations is a growing area of interest. One important class of problems involves steady state diffusion. To study these cases, a grand canonical molecular dynamics approach has been developed by Heffelfinger and van Swol [J. Chem. Phys., 101, 5274 (1994)]. With this method, the flux of particles, the chemical potential gradients, and density gradients can all be measured in the simulation. In this paper, we present a complementary approach that couples a nonlocal density functional theory (DFT) with a transport equation describing steady-state flux of the particles. We compare transport-DFT predictions to GCMD results for a variety of ideal (color diffusion), and nonideal (uphill diffusion and convective transport) systems. In all cases excellent agreement between transport-DFT and GCMD calculations is obtained with diffusion coefficients that are invariant with respect to density and external fields.

*corresponding author

DISCLAIMER

I. INTRODUCTION

Molecular scale diffusion plays an important role in a wide variety of systems including polymer degredation, catalysis, membrane separations, and ion transport through biological membranes. In all of these cases, understanding diffusive processes on a molecular scale will provide the ability to engineer these systems as desired.

The primary computational approaches that have been applied to molecular diffusion are molecular dynamics (MD) simulation [1,3–5,2] and transition state theory (TST) [6,7]. TST has been most often applied to rare event diffusion where the diffusing species is dilute, and the potential energy barriers between different states are high. A few recent efforts are focusing on the calculation of diffusive free energy barriers in the presence of a solution or multiple diffusing particles [8]. MD approaches include both linear response theory as coupled with equilibrium MD calculations [1,2], and non-equilibrium molecular dynamics (NEMD) methods [9]. MD has been applied to a wide range of diffusion problems including diffusion in zeolites [10,11], amorphous membranes [4,12], nanoporous carbon materials [13], and polymers [14,15].

The particular NEMD method we have applied is grand canonical molecular dynamics (GCMD) [3–5,16]. In GCMD, an overall chemical potential driving force is maintined and particle flux is measured. A transport law with some assumed functional form is then used to estimate diffusion coefficients. Typically Fick's law [3,5,11,16,17],

$$J_\alpha = -D_\alpha \nabla \rho_\alpha, \tag{1}$$

is applied where J is the flux of species α, D is the diffusion coefficient, and ρ is a number density.

While GCMD provides an exact computer experiment for studying diffusion, the calculations (as with most molecular simulations) are quite expensive to perform. It is therefore desireable to develop complementary approaches for steady state non-equilibrium systems that are based on molecular theories. In this paper we present the results of coupling a nonlocal density functional theory (DFT) to a transport equation, and solving the system of equations under steady state conditions.

In section II, the transport-DFT approach is presented, in section III, DFT and GCMD calculations are compared for a variety of model systems, and in section IV a summary of our conclusions is presented. In general, good agreement is found between transport-DFT and GCMD approaches; however, transport-DFT calculations are $O(10^5)$ times faster than the GCMD calculations. Therefore, this new transport-DFT approach provides a powerful addition to the tools available for studying molecular steady state transport.

II. MODEL AND THEORY

For the GCMD calculations presented here, the underlying molecular model describing fluid-fluid interactions is the Weeks-Chandler-Anderson (WCA) fluid which is based on a cut and shifted 12-6 Lennard-Jones (LJ) potential [18], $u(r) = u_{LJ}(r) - u_{LJ}(r_c)$, where

$$u_{LJ}(r) = 4\epsilon \left[\left(\frac{\sigma}{r}\right)^{12} - \left(\frac{\sigma}{r}\right)^{6} \right], \tag{2}$$

σ is the diameter of the solvent molecule, ϵ is the energy parameter controlling the strength of fluid-fluid interactions, and r_c is the cutoff distance for the potential. For a WCA fluid, the LJ potential is reduced to only the repulsive part of the LJ potential since the cut-off is taken at the potential minimum, $r_c/\sigma \approx 1.122$.

DFT approaches are generally based on the assumption of chemical equilibrium, and a free energy functional, Ω is minimized with respect to the density distrbution, $\rho(\mathrm{r})$ at constant chemical potential, μ. We relax this condition, and assume instead that steady state is equivalent to a condition of *local* equilibrium where the chemical potential varies spatially. In this case, the energy minimization we perform is

$$\left(\frac{\delta\Omega}{\delta\rho(\mathrm{r})}\right)_{\mu(\mathrm{r}),T} = 0. \tag{3}$$

Fluid density distributions in the cases considered here are inhomogeneous spatially due to nonuniform boundary conditions. In the cases discussed in section IIID, external fields lead to more pronounced inhomogeneities in the fluid. Thus, the grand canonial free energy is

$$\Omega = F_{id} + F_{hs} - \sum_\alpha \int d\mathrm{r}\ \rho_\alpha(\mathrm{r}) \left[\mu_\alpha(\mathrm{r}) - V_\alpha^{ext}(\mathrm{r})\right]. \tag{4}$$

where the sum is taken over all the species in the system, V^{ext} is the external field (zero in all cases except section IIID), the ideal and excess hard sphere free energy contributions are

$$F_{id} = kT \sum_\alpha \int d\mathrm{r}\ \rho_\alpha(\mathrm{r}) \left\{ \ln\left(\Lambda^3 \rho_\alpha(\mathrm{r})\right) - 1 \right\}, \tag{5}$$

and

$$F_{hs} = \int d\mathrm{r}\ \Phi\{\bar{\rho}_\gamma(\mathrm{r})\} \tag{6}$$

respectively, Λ is the de Broglie wavelength, Φ is the free energy density of the hard sphere fluid, and $\bar{\rho}_\gamma$ are nonlocal densities. In calculating the hard sphere contribution, we have applied the nonlocal formulation of Rosenfeld that is detailed in the appendix [19].

The functional minimization of Eq.3 produces the Euler-Lagrange equations

$$\mu_\alpha(\mathbf{r}) = kTln\rho_\alpha(\mathbf{r}) + \int d\mathbf{r}' \sum_\gamma \frac{\partial \Phi}{\partial \bar{\rho}_\gamma} w^{(\gamma)}(|\mathbf{r}-\mathbf{r}'|) + V_\alpha^{ext} \tag{7}$$

which can be solved at each point in the domain for the steady state density distrubutions, $\rho_\alpha(\mathbf{r})$ for a given $\mu_\alpha(\mathbf{r})$.

We are interested in steady state diffusion where $\mu(\mathbf{r})$ is not known a priori, but rather satisfies a known diffusion equation. Steady state is defined by a time independent mass balance consisting only of the divergence-free condition on the total flux,

$$\nabla \cdot J = 0. \tag{8}$$

The total flux may be attributed to a variety of physical effects as is discussed in detail by Mason and Lonsdale [20] in the context of membrane transport. For diffusion in binary solutions in the absence of both a membrane and pressure gradients, the two transport equations are

$$\frac{\rho_2}{\rho D_{12}}(\mathbf{u}_1 - \mathbf{u}_2) = -\frac{1}{RT}\nabla\mu_1 \tag{9}$$

and

$$\frac{\rho_1}{\rho D_{21}}(\mathbf{u}_2 - \mathbf{u}_1) = -\frac{1}{RT}\nabla\mu_2 \tag{10}$$

where $\mathbf{u}$ is the particle velocity, and $\rho = \rho_1 + \rho_2$. In this paper, we further simplify our discussion by considering primarily color diffusion (with the exception of section IIIB). In color diffusion, all the particles are identical in size and interactions, they differ only by the species number (or color) they are assigned. In this case, $D_{21} = D_{12} = D_{11} = D_{22} = D$, and we assume that the diffusion coefficient is spatially invariant in solving the transport-DFT problem.

Any center of mass motion in the system, J_{CM} is defined by

$$J_{CM} = J_1 + J_2 = \rho_1 u_1 + \rho_2 u_2 \tag{11}$$

and combining Eqs.11 with 9 or 10 it is straightforward to show that the flux may be defined as

$$J_\alpha = -D\rho_\alpha \nabla\mu_\alpha + \bar{v}\rho_\alpha \tag{12}$$

where $\bar{v}$ is the mean particle velocity in the fluid. Note that the diffusive contribution to the flux is not Fick's law (Eq.1).

The chemical potential of a given species can be written as a sum of ideal, excess hard sphere, and external field contributions,

$$\mu = \mu_{id} + \mu_{hs} + V^{ext}, \tag{13}$$

as shown in Eq.7. If $V^{ext} = 0$, *and* there are no nonideal contributions to the flux, (e.g. $\mu_{hs} = 0$ or $\nabla\mu_{hs} = 0$), then only the ideal contribution ($\nabla\mu_{id} = kT\nabla\rho/\rho$) is present, and Fick's law

$$J_\alpha = -D\nabla\rho_\alpha, \tag{14}$$

is recovered.

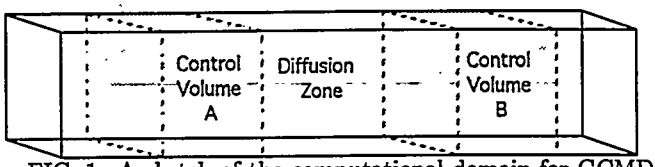

FIG. 1. A sketch of the computational domain for GCMD simulations. Periodic boundary conditions are applied in all dimensions, and chemical potential control is maintained in the two control volumes in the shaded regions.

The two contributions to the flux in Eq.12 are diffusive and convective fluxes respectively. The convective term is written in terms of a mean velocity implying that we are considering cases of plug flow where the velocity field is homogeneous. For more complex flows, velocity distributions must be solved simultaneously with the transport-DFT described here. Such calculations have been previously performed (without diffusive transport) for cases of Couette flow and Poiseuille flow [21].

In the following sections we test the transport-DFT approach outlined above by explicit comparison with GCMD simulations in a variety of situations. We discuss the magnitude and type of errors that can develop when Fick's law (Eq.14) is used to analyze data from GCMD simulations. We also show that the transport-DFT approach can be applied in cases where pressure gradients and external fields are present.

III. RESULTS

In this section, we will compare GCMD calculations to the predictions of the steady-state DFT described above. We begin with a brief description of the GCMD method.

In GCMD calculations, the simulation volume is split into two control volumes and two diffusion zones as sketched in Fig.1 One of the diffusion zones is split between the ends of the box (in the x-direction) where there are periodic boundary conditions. The total system size for calculations presented here is $60\sigma \times 10\sigma \times 10\sigma$.

The GCMD calculations were done on the massively parallel ASCI-Red Tflops computer (composed of 200 MHz Pentium Processors) at Sandia National Laboratories using the parallel code LADERA. The LADERA code is parallelized using a spatial decomposition, and has been discussed elsewhere [14,22]. All the calculations presented here were performed on 48 processors with each processor owning a cube that is 5σ on edge (ie. the processors have a spatial decomposition of $12\times2\times2$). Every processor that owns pieces of the control volumes split their volumes into eight sub-domains. One insertion/deletion cycle involves an attempted insertion or

deletion in each of the eight subdomains on all of the processors. Hence for the chosen geometry and processor array, one grand-canonical (GC) cycle is composed of 128 insertions/deletions total [23].

The geometry in Fig.1 allows for variations in the equilibrium properties (e.g. $< \rho >$) only in the x-direction. Therefore the DFT calculations are reduced to solving for density and chemical potential profiles in only one dimension (1D). Our numerical solution (discussed elsewhere in the context of equilibrium 2D and 3D problems [24,25]) combines a collocation approach to the Euler-Lagrange equations with a Garlerkin finite element approach for the transport equation. Linear basis functions were used for the discretization, and a fully coupled Newton method was used to solve for the steady-state solution. The DFT calculations were run in serial on a 433 MHz DEC Alpha workstation.

A. Color Counter-Diffusion

We begin with color counter-diffusion where there are two species with identical properties. Each particle is labeled (or colored) by its assigned species number (1,2). To set up equal counter-diffusion, we set $\mu_1^L = \mu_2^R$ and $\mu_2^L = \mu_1^R$ where the superscripts R and L refer to the right and left control volumes respectively.

The case of color diffusion is unique in that Eq.14 and Eq.12 are identical regardless of the fluid density. This result stems from the fact that $\bar{v} = 0$ and the total density is constant everywhere in the simulation volume. As a result, $\nabla \mu_{hs} = 0$, and only the ideal term contributes to the flux.

We considered two cases of color diffusion. Both are WCA fluids with a temperature of $kT/\epsilon = 1$, but the two cases have different total densities. The chemical potential set points in the control volumes for the first case were $\mu_1^L/kT = 1.54$ and $\mu_2^L/kT = 2.34$, while they were $\mu_1^L/kT = 3.0$ and $\mu_2/kT = 6.0$ for the second case.

The GCMD simulations were composed of 100,000 MD time-steps for equilibriation and 400,000 MD time-steps for accumulating averages. The time increment for the integration of Newton's equations of motion was $\Delta t = 0.01$, and 10 GC cycles were attempted at every 10th MD time-step. The total run time on the parallel computer was approximately 3 hours. For comparison, the DFT results converged in less than 10 Newton iterations in about 5 seconds on a workstation.

Figures 2 and 3 compare GCMD and transport-DFT density and chemical potential profiles for the two cases described above. The boundary conditions on the DFT calculations were chosen to match the densities observed in control volumes of the GCMD calculations ($-15 < x/\sigma < -10$ and $10 < x/\sigma < 15$). The chemical potentials from DFT calculations do not match GCMD set points, but rather are shifted down in both cases. This shift arises because the DFT assumes the WCA fluid can

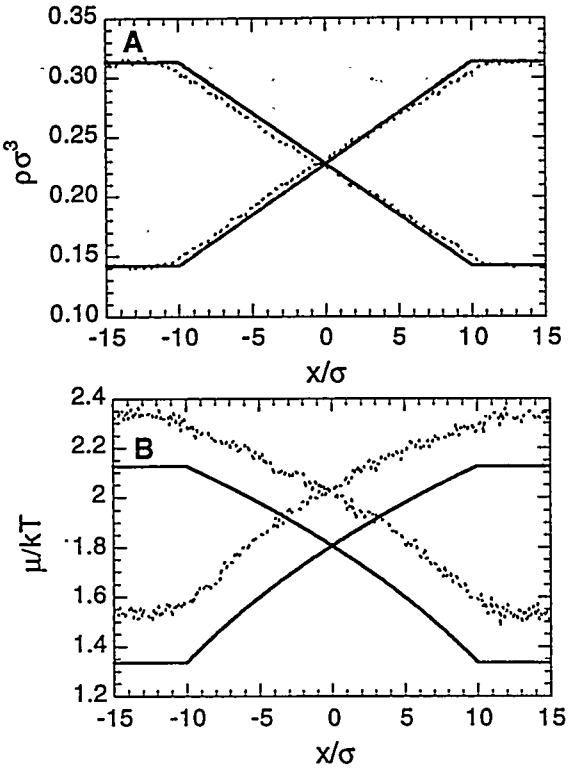

FIG. 2. Density ($\rho\sigma^3$) profiles (A) and chemical potential (μ/kT) profiles (B) in a diffusion zone. The total density is $\rho_{tot}\sigma^3 \approx 0.45$ Solid lines are transport-DFT results; dotted lines are GCMD results

be treated as a hard sphere fluid, and because the equation of state (Percus-Yevik) is not exact. Considering the diffusion zone in each case, it is apparant that DFT predictions of the density profiles and chemical potential *gradient* profiles reproduce GCMD simulations very well.

The success of the transport-DFT in reproducing $\rho(x)$ and $\nabla\mu(x)$ is significant because it demonstrates that the DFT and GCMD approaches will yield consistent flux predictions. Thus if one wants to predict the variation of the flux through a range of parameters, it is possible to perform only a few GCMD calculations to establish the bounds for the diffusion coefficient. DFT calculations may then be performed to determine the flux through a wider range of system parameters.

To illustrate the equivalence of Eq.12 and Eq.14 for color counter diffusion, Fig.4 compares GCMD $\rho d\mu/dx$ and $d\rho/dx$ profiles to the DFT prediction of $\rho d\mu/dx$. The GCMD estimates of $d\rho/dx$ were found both from an overall fit to the density profile, and by applying central finite differences (CFD) performed on 1σ increments of the $\rho(x)$ data. The GCMD estimates of $\rho d\mu/dx$ are based on CFDs perfomed on 1σ increments of *smoothed* chemical potential profiles.

All the estimates of J/D in Fig.4 are consistent with one another, but the GCMD/CFD estimations of $\rho d\mu/dx$

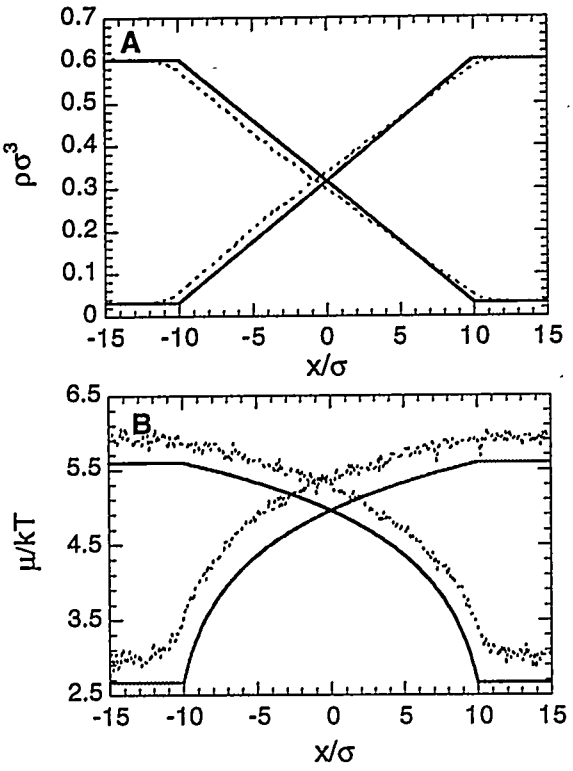

FIG. 3. Same as Fig.2 except that the total density is $\rho_{tot}\sigma^3 \approx 0.64$

and $d\rho/dx$ have the largest uncertainties due to statistical noise in the data. Therefore, the highest presicion GCMD estimates of diffusion coefficient come from taking the overall slope of the density profile, and applying Fick's law. However, as we will show in the following sections there are many cases where either the nonideal contributions to the chemical potential will contribute to the flux (section IIIB) or where external fields will cause the density profile to have a complex structure (section IIID). These cases will make application of Fick's law difficult.

B. Uphill Diffusion

One case where Fickian diffusion is clearly incorrect may be found in studies of *uphill* diffusion. It has been observed in GCMD studies of ternary systems, that chemical potential and density gradients can have slopes with opposite sign [17]. In these cases, the measured particle flux always goes in the direction of decreasing chemical potential. So from a Fickian point of reference, the diffusion appears to be uphill. Several experimental observations of uphill diffusion have been reported as well [26,27].

In this section we consider application of the transport-DFT approach to non-ideal ternary systems. We assume that there is no center of mass motion in this system.

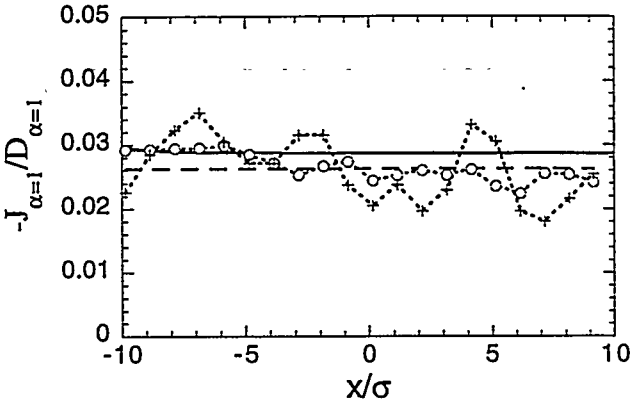

FIG. 4. The flux divided by the diffusion coefficient in the central diffusion zone of Fig.3. The various curves are: DFT prediction of $\rho d\mu/dx$ (solid line), GCMD calculation of $d\rho/dx$ based overall slope of density profiles (dashed line), GCMD CFD calculation of $\rho d\mu/dx$ (+), GCMD CFD calculation of $d\rho/dx$ (o).

We further assume that the transport law given in Eq.12 is valid for this ternary system. This formulation of the flux may not be optimal for the non-ideal ternary systems discussed here. However, for the purposes of this discussion we only seek to demonstrate that nonideal behaviors such as uphill diffusion can be found using the transport-DFT approach, and estimate how such nonidealities may affect estimates of the driving force.

Both the mixing rules for interaction diameters, σ_{ij} and our control volume densities were chosen based on previous GCMD studies of uphill diffusion [17]. More specifically the interaction diameters were, $\sigma_{ij} = \sigma_k$ where $k = Min(i,j)$. In the particular case we present here, the matrix of interaction diameters was

$$\begin{array}{c} \\ \sigma_1 \\ \sigma_2 \\ \sigma_3 \end{array} \begin{array}{c} \begin{array}{ccc} \sigma_1 & \sigma_2 & \sigma_3 \end{array} \\ \begin{pmatrix} 1.0 & 1.0 & 1.0 \\ 1.0 & 1.3 & 1.3 \\ 1.0 & 1.3 & 1.5 \end{pmatrix} \end{array}. \qquad (15)$$

Transport-DFT results in Fig.5 show similar behavior as was observed in GCMD simulations [17] where the slope of the density and chemical potential profiles of component 2 have opposite sign. This uphill diffusion result shows that the transport-DFT approach may be useful in analyzing transport in complex multicomponent mixtures as well as the simple binary systems of the previous section.

The nonidealities in these mixtures lead to nonzero contributions to the flux from $\nabla\mu_{hs}$. The result is that the density profiles are not linear. Thus, a local application of Fick's law would predict a spatially varying diffusion coefficient while a more global analysis based on the overall slope between the control volumes would not have the precision of the color counter diffusion case in Fig.4.

Table I details the difference between $\rho\nabla\mu$ and the global approach to $\nabla\rho$ based on the results in Fig.5. The

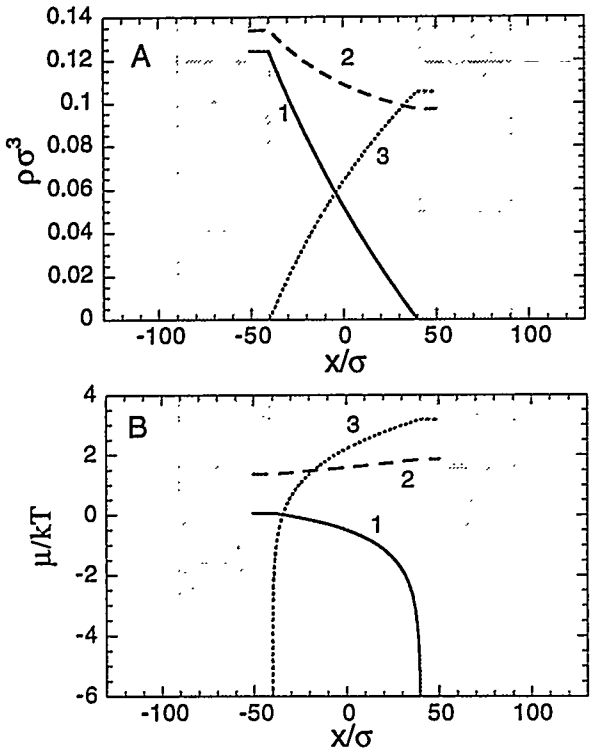

FIG. 5. Density (A) and chemical potential(B) profiles for a case of uphill diffusion. The curves are labeled by the component number, and the the x-axis is scaled for ease of comparison with Figs. 2 and 3 of Thompson *et.al*[21]. The grey regions indicate where the control volumes were located in GCMD calculations. In locating this particular case, σ_2 and σ_3 were varied in the range $\sigma_{2,3}/\sigma_1 = 1.0 - 1.6$. For all values of σ_2, a transition in component 2 from downhill diffusion to uphill diffusion occured at $\sigma_3/\sigma_1 \approx 1.45$.

nonidealities in the system now contribute to a 20-40% difference between these two estimations of diffusive driving forces even for components 1 and 3 where downhill diffusion is observed.

C. Pressure Driven Diffusion

We now turn to cases where convective transport occurs simultaneously with diffusive transport, and we begin with pressure driven diffusion. Once again binary color mixtures are used for the calculations.

GCMD calculations were performed by setting the chemical potential of both species in the left control volume to $\mu_1^L/kT = \mu_2^L/kT = 3.0$ and the chemical potential of species 1 in the right control volume to $\mu_1^R = 2.0$. The chemical potential of species 2 in the right control volume varied from $\mu_2^R/kT = 4$ (case A) to $\mu_2^R/kT = 3.5$ (case B), to $\mu_2^R/kT = 3$ (case C). In case A, the pressure in the right control volume is higher than the left; in case C, the pressure imbalance is reversed; and in case B, there is almost no pressure drop.

Species	$d\rho/dx$	$\rho d\mu/dx$	% difference
1	-0.0015	-0.0012	25%
2	-0.00044	0.00067	166%
3	0.0013	0.0021	38%

TABLE I. A comparison of J/D using Fick's law (Eq.8) and Eq.9 to describe diffusion for each of the three species in the transport-DFT calculations of the ternary system detailed in Fig.5.

100,000 MD time-steps were performed for equilibriation, and 600,000 MD time-steps were used for accumulating averages. The time increment for the integration of Newton's equations of motion was $\Delta t = 0.01$, and 20 GC cycles were attempted at every 5th MD time-step. The total run time per solution was approximately 14 hours.

Equilibration of GCMD profiles is more difficult in these cases than the previous color diffusion example due to the particle acceleration that accompanies the pressure gradient. Steady-state is achieved as a result of the effective friction in the control volumes that arises from the insertions and deletions of particles. These particle insertions are accompanied by velocity randomization that provides the needed friction.

Figures 6 and 7 show the density and chemical potential profiles from GCMD and transport-DFT calculations where both diffusive and convective terms are included in DFT calculations For comparison, DFT calculations without the convective flux term are also included in the figures. Inclusion of the center of mass motion (or convective terms) is crucial to reproducing GCMD results with the transport-DFT approach.

The small discontiuities in $\mu(x)$ in the GCMD calculations, seen at $x/\sigma = 10$ in Fig.7A and $x/\sigma = -10$ in Fig.7C show that the pressure drop, and therefore the acceleration, occur almost instantaneously and not over the whole domain. This feature justifies the use of a constant velocity convective flux, and is supported by the excellent agreement with transport-DFT calculations.

D. External Fields

Finally we consider transport of the binary tagged by color particles in the presence of external fields. This is a particularly important case since transport through any porous media involves an external field composed of the interactions of the fluid particles with the porous media. We consider an external field representative of a simple porous membrane with the form $V^{ext} = v(|x|) - v(|x|_{cut})$ when $|x| > |x|_{min}$ and $V^{ext} = v(|x|_{min}) - v(|x|_{cut})$ when $|x| \leq |x|_{min}$ where

$$v/kT = \epsilon_{wf}\left[\frac{2}{15}\left(\frac{\sigma}{|x|}\right)^9 - \left(\frac{\sigma}{|x|}\right)^3\right], \qquad (16)$$

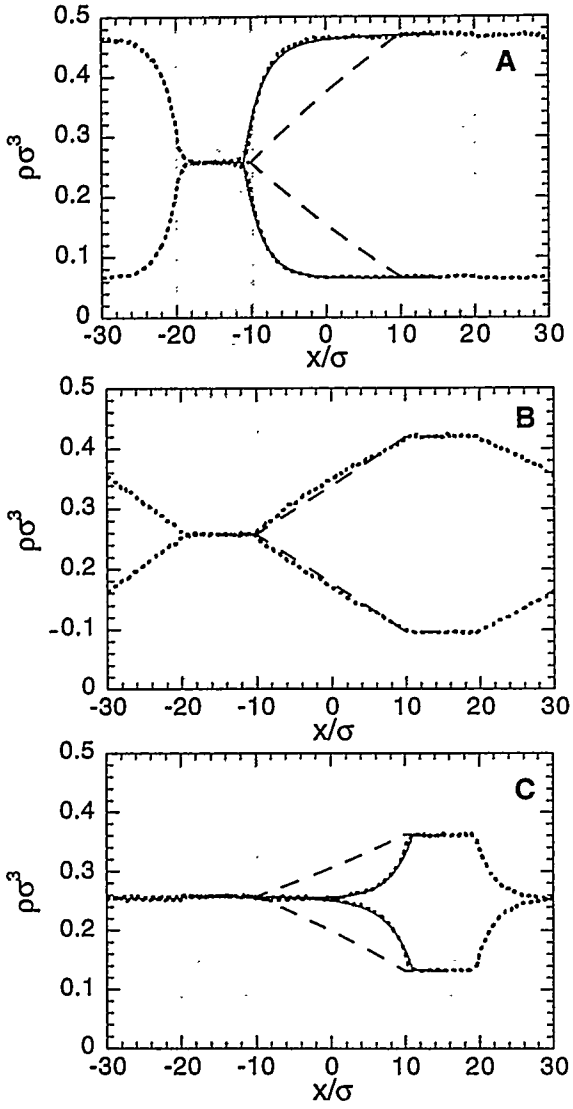

FIG. 6. Density profiles for both GCMD (dotted lines) and steady state DFT (solid and dashed lines) calculations. DFT results in dashed lines include only the diffusive flux while solid lines innclude the convective term as well. The three cases have $\mu^R/kT = 4.0$ (A), $\mu^R/kT = 3.5$, and $\mu^R/kT = 3.0$ (C). In all cases, the densities in the left control volume for both species are $\rho_i\sigma^3 = 0.258 \pm 0.001$ ($\rho\sigma^3 = 0.516$). The densities on the right hand side vary from $\rho_1\sigma^3 = 0.471$, $\rho_2\sigma^3 = 0.067$, and $\rho\sigma^3 = 0.538$ (A); to $\rho_1\sigma^3 = 0.419$, $\rho_2\sigma^3 = 0.096$, and $\rho\sigma^3 = 0.515$ (B); to $\rho_1\sigma^3 = 0.362$, $\rho_2\sigma^3 = 0.131$, and $\rho\sigma^3 = 0.493$ (C).

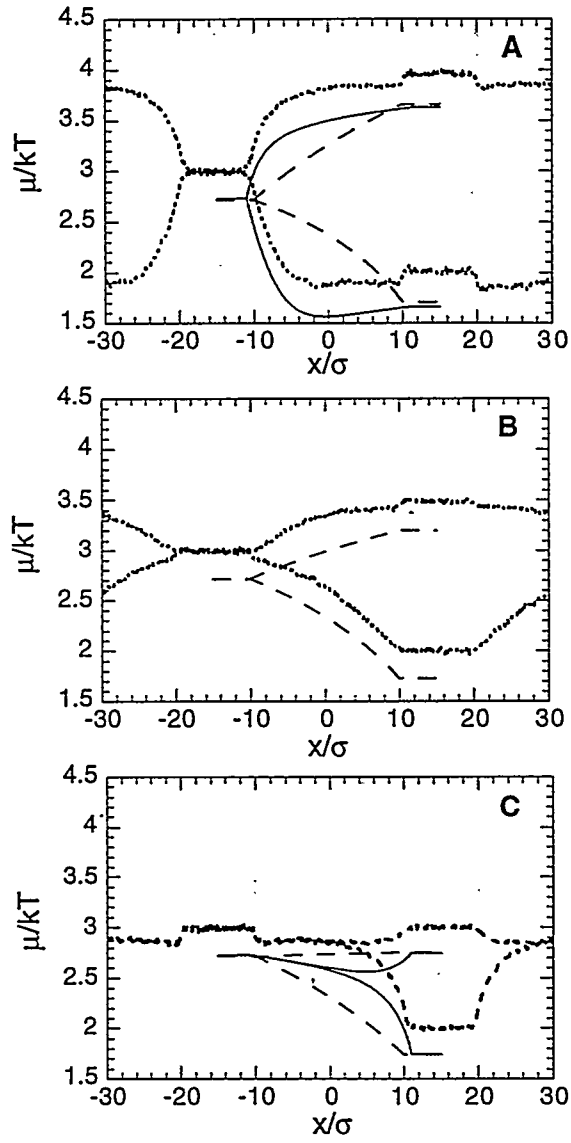

FIG. 7. Chemical potential profiles corresponding to the density profiles results in Fig.6.

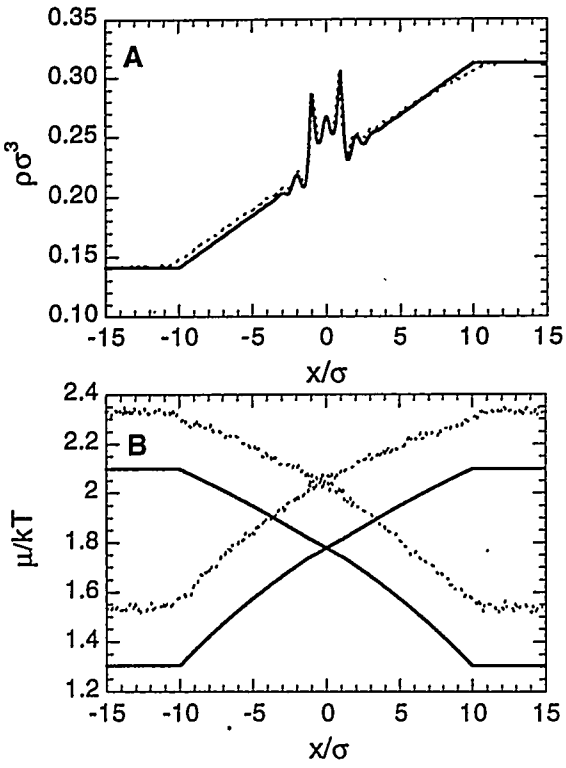

FIG. 8. Density ($\rho\sigma^3$) profiles (A) and chemical potential (μ/kT) profiles (B) in a diffusion zone where there is an external field centered at $x = 0$ that is attractive to both species. Solid lines are transport-DFT results, dotted lines are the results of GCMD simulations.

$|x|_{cut} = 2.5\sigma$, and $|x|_{min}$ is the distance where the potential is a minimum.

We consider two cases. In the first, $\epsilon^{\alpha}_{wf}/\epsilon = \epsilon^{\beta}_{wf}/\epsilon = 1.0$ so both species (α, β) are equally attracted to a potential energy well at $|x| = 0$. In the second case, $\epsilon^{\alpha}_{wf}/\epsilon = 1.0$ and $\epsilon^{\beta}_{wf}/\epsilon = -1.0$. In this case species β must overcome a potential energy barrier that inhibits its transport. In the first case, the symmetric nature of the problem leads once again to zero net motion of the center of mass of the system, while in the second case, species α can be expected to dominate the tranport creating a net center of mass motion.

Figure 8 shows density and chemical potential profiles respectively for the case where both species experience the same external field. Only one species is shown in 8A for clarity of presentation. As expected, adsorption is observed in the center region due to the external field, and density oscillations are due to the solvent packing constraints. Clearly application of Fick's law in the vicinity of these density oscillations cannot yield sensible results.

The chemical potential profiles in Fig.8B appear to be very similar to those in Fig.1B. However, transport-DFT calculations were based on Eq.12 so the density oscillations in Fig.8A must be balanced by oscillations in $\nabla\mu$.

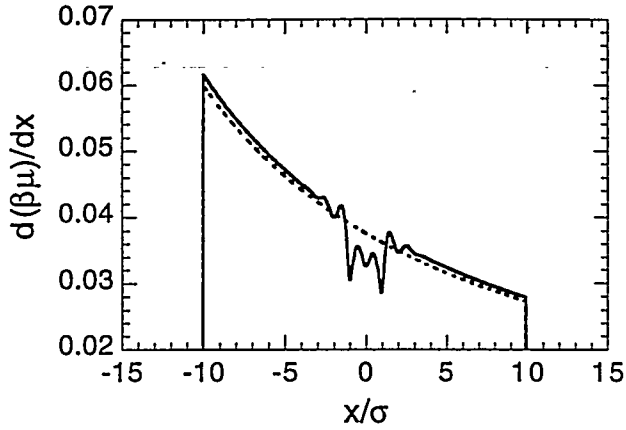

FIG. 9. Chemical potential gradient, $\nabla\mu$ profiles corresponding to transport-DFT profiles in Fig.8B (solid lines) and Fig.2B (dashed lines).

In fact, when $\nabla\mu(x)$ is plotted (see Fig.9) the oscillations are apparant. The statistical noise on the GCMD calculations will likely prevent accurate computation of $\nabla\mu$ in many cases where external fields are present. Thus, in some cases it may be useful to combine the transport-DFT and GCMD approaches for an estimation of diffusion coefficient. The DFT provides an estimate of the driving force while the GCMD provides a measure of the flux. Together a prediction of diffusion coefficient can be obtained.

When the external field is attractive to one species and repulsive to the other, both diffusive and convective transport are important. In transport-DFT calculations, the ratio, $\bar{v}/D$ was adjusted for the best match of GCMD and DFT calculations. Since $\bar{v}$ is directly measured in GCMD calculations, obtaining an estimate of the diffusion coefficient given the matching parameter is straightforward. Fig.10 shows density and chemical potential profiles for our example of this situation. The density of the one adsorbed species in the center region is now significantly higher than it was even in Fig.8A. The other species shows significant exclusion from the central region as is evidenced by its low density. Again, there is good agreement between GCMD and transport-DFT calculations of both $\rho(x)$ and $\nabla\mu(x)$.

The excellent agreement between transport-DFT and GCMD calculations for the cases in this section are particularly remarkable as transport-DFT calculations are based on spatially invariant diffusion coefficients. Calculations of diffusion through pores have shown that surface effects can alter (usually decrease) the magnitude of the diffusion coefficient [28]. Clearly, the application of the transport-DFT approach to porous systems will require a more thorough investigation.

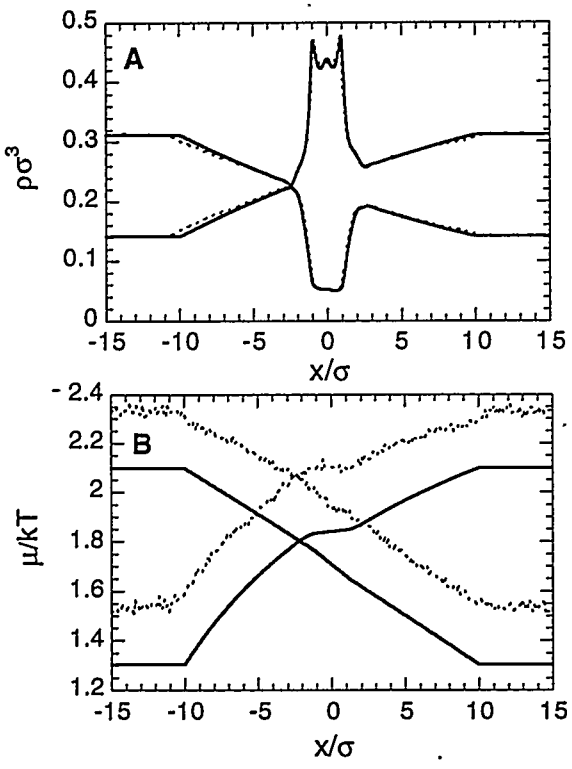

FIG. 10. Density ($\rho\sigma^3$) profiles (A) and chemical potential (μ/kT) profiles (B) in a diffusion zone where there is an external field centered at $x = 0$ that is attractive to only one species and repulsive to the other. Solid lines are transport-DFT results, dotted lines are results of GCMD simulations.

Figure	J_α	J_β	D_α	D_β
1	-0.0024	0.0025	0.28	0.29
8	-0.0026	0.0024	0.30	0.28
10	-0.0054	-0.00016	0.30	0.27

TABLE II. A comparison of diffusion coefficients for several of the cases investigated in this paper (as indicated by the figure number).

E. Diffusion Coefficients

Finally, we present calculations of diffusion coefficients that combined flux measurements from GCMD simulations with driving forces from transport-DFT. Results for the cases that were presented in Figs.1, 8, and 10 are shown in Table II. These cases all have the same overall chemical potential driving forces, but the fluid particles experience very different external fields in the diffusion zone. The predicted diffusion coefficient is found to be constant within the errors associated with flux measurments among all the cases.

IV. CONCLUSIONS

To summarize, we have presented a novel approach to studying molecular steady-state transport. This approach couples a molecular theory, DFT, with a diffusive (and in some cases convective) transport law in order to predict density and chemical potential gradients in nonequilibrium steady-state systems for several simple mixtures.

The results of transport-DFT calculations were compared explicitly with grand canonical molecular dynamics simulations(GCMD) for a variety of systems. We found that the two methods were in agreement for predictions of both chemical potential and density profiles given the assumption of a spatially invariant diffusion coefficient provided that the center of mass motion of the system was known. Thus given a diffusion coefficient, both methods will yield the same flux. In order to compute the flux as a function of system parameters efficiently, only a few GCMD calculations are needed to determine the bounds on diffusion coefficients. The transport-DFT approach may then be used for exploring a complete range of the parameters of interest.

The agreement we found was based on the application of a local transport law, $J = -D\rho(x)\nabla\mu(x)$. Fick's law, $J = -D\nabla\rho(x)$ was demonstrated to be incorrect locally for cases where an external field is present and globally for a case of nonideal *uphill* diffusion.

Given the efficiency of transport-DFT calculations, this new transport-DFT approach may provide a powerful addition to the tools available for studying molecular steady state transport and its effects on complex surface phenomena such as capillary condensation and wetting.

V. APPENDIX

In the nonlocal DFT of Rosenfeld [19], the hard sphere free energy density, Φ, was derived from scaled particle theory in terms of the nonlocal densities, $\bar{\rho}_\gamma$. These nonlocal densities are

$$\bar{\rho}_\gamma(\mathbf{r}) = \sum_\alpha \int d\mathbf{r}' \rho_\alpha(\mathbf{r}') w_\alpha^{(\gamma)}(|\mathbf{r}-\mathbf{r}'|). \tag{17}$$

where the summation is taken over the species, α. The weight functions, $w_\alpha^{(\gamma)}$, are

$$\begin{aligned} w_\alpha^{(3)}(r) &= \Theta(r-R_\alpha) \\ w_\alpha^{(2)}(r) &= 4\pi R_\alpha w_\alpha^{(1)}(r) = 4\pi R_\alpha^2 w_\alpha^{(0)}(r) = \delta(r-R_\alpha) \\ w_\alpha^{(V2)}(r) &= 4\pi R_\alpha w_\alpha^{(V1)}(r) = (\mathbf{r}/r)\delta(r-R_\alpha) \end{aligned} \tag{18}$$

where the $\mathbf{r}$ indicates a vector. These weight functions are based on the geometry of the fluid particles as Θ is the step function, δ is the Dirac delta function, and R is the radius of a particle. Thus the integrals over weight functions are related to the volume, surface area, and radius of the particle. Note that w^{V1} and w^{V2} are vectors, and so the hard sphere free energy density is a sum of scalar and vector contributions, $\Phi = \Phi_s + \Phi_v$, with

$$\begin{aligned} \Phi_s &= -\bar{\rho}_0 ln(1-\bar{\rho}_3) + \frac{\bar{\rho}_1\bar{\rho}_2}{1-\bar{\rho}_3} + \frac{1}{24\pi}\frac{\bar{\rho}_2^3}{(1-\bar{\rho}_3)^2} \\ \Phi_v &= -\frac{\bar{\rho}_{V1}\cdot\bar{\rho}_{V2}}{1-\bar{\rho}_3} - \frac{1}{8\pi}\frac{\bar{\rho}_2(\bar{\rho}_{V2}\cdot\bar{\rho}_{V2})}{(1-\bar{\rho}_3)^2}. \end{aligned} \tag{19}$$

VI. ACKNOWLEDGEMENTS

The authors would like to thank Grant Heffelfinger for many helpful disscussions.

Sandia is a multiprogram laboratory operated by Sandia Corporation, a Lockheed Martin Company, for the United States Department of Energy under Contract DE-AC04-94AL85000.

[1] E.J. Maginn, A.T. Bell, and D.N. Theodorou, J. Phys. Chem., **97**, 4173 (1993).
[2] D. Nicholson, J. Membrane Sci., **129**, 209 (1997).
[3] G.S. Heffelfinger and F. van Swol, J. Chem. Phys., **101**, 5274 (1994).
[4] J.M.D. MacElroy, J. Chem. Phys., **101**, 5274 (1994).
[5] D. Nicholson and R. Cracknell, Langmuir, **12**, 4050 (1996).
[6] R.L. June, A.T. Bell, and D.N. Theodorou, J. Phys. Chem., **95**, 8866 (1991).
[7] A.A. Gusev and U.W. Suter, J. Chem. Phys., **99**, 2228 (1993).
[8] C. Tunca and D.M. Ford, J.Chem.Phys., in press.
[9] P.T. Cummings and D.J. Evans, Ind. Eng. Chem. Res., **31**, 1237 (192).
[10] J.M.D. MacElroy and S.-H. Suh, in *Progress in Zeolite and Microporous Materials*, ed. H. Chon, S.-K. Ihm, and Y.S. Uh, Elsevier (1997).
[11] S. Fritzsche, R. Haberlandt, and J. Kärger, Zeitschrift für Physikalische Chemie, **189** 211 (1995).
[12] S.-J. Marrink and H.J.C. Berendsen, J. Phys. Chem., **98**, 4155 (1994).
[13] L. Xu, M.G. Sedigh, M. Sahimi, and T.T. Tsotsis, Phys. Rev. Lett., **80**, 3511 (1998).
[14] D.M. Ford and G.S. Heffelfinger, Mol. Phys., **94**, 673 (1998).
[15] S. Sunderrajan, C.K. Hall, and B.D. Freeman, J.Chem.Phys., **105**, 1621 (1996).
[16] W. Dong and H.Luo, Phys. Rev. E, **52** 801 (1995).
[17] A.P. Thompson, D.M. Ford, and G.S. Heffelfinger, J. Chem. Phys., **109**, 6406 (1998).
[18] J.D. Weeks, D. Chandler, and H.C. Anderson, J. Chem. Phys., **54**, 5237, (1971).
[19] Y. Rosenfeld, Phys. Rev. Lett., **63**, 980 (1989).
[20] E.A. Mason and H.K. Lonsdale, J. Membrane Science, **51**, 1 (1990).
[21] I. Bitsanis, T.K. Vanderlick, M. Tirrell, H.T. Davis, J. Chem. Phys., **89**, 3152 (1988).
[22] G.S. Heffelfinger and D.M. Ford, Mol. Phys., **94**, 659 (1998).
[23] G.S. Heffelfinger and M.E. Lewitt, J. Comp. Chem., **17**, 250 (1996).
[24] L.J. Douglas Frink and A.G. Salinger, J.Chem.Phys., **110**, 5969 (1999).
[25] L.J. Douglas Frink and A.G. Salinger, submitted to J. Comp. Phys. (1999).
[26] J.B. Duncan and H.L. Toor, A.I.Ch.E. J., 8 38 (1962).
[27] S. Tsuchiya and M. Senō, J. Phys. Chem., **98**, 13680 (1994).
[28] M. Schoen, J.H. Cushman, D.J. Diestler, and C.L. Rhykerd, Jr., J. Chem. Phys., **88**, 1394 (1988).